Microscopy and Microanalysis, 2026, **32**, ozag029
https://doi.org/10.1093/mam/ozag029
Advance access publication 2 June 2026
Original Article

Microscopy AND Microanalysis

Dark Field Colored Imaging of Rat Bone Shows the Variation of Nanocrystal Orientation Within and Between Mineral Platelets

Artem Bibko[1], Henry Schwarcz[2,3,*], and Viktória Kovacs Kis[4,5]

[1]*Tomsk State University, Department of Mineralogy and Geochemistry, Lenina avenue, 36, Tomsk 634050, Russia*
[2]*School of Earth, Environment and Society, McMaster University, Hamiton, Ontario, Canada L8S 4K1*
[3]*School of Biomedical Engineering, McMaster University, Hamilton, Ontario, Canada L8S 4K1*
[4]*Thin Film Physics Laboratory, HUN-REN Centre for Energy Research, Konkoly-Thege Miklós u. 29-33, Budapest 1121, Hungary*
[5]*Department of Mineralogy, Eötvös Loránd University, Pázmány Péter sétány 1/c, Budapest 1117, Hungary*

***Corresponding author:** Henry Schwarcz, Email: schwarcz@mcmaster.ca

Abstract

Bone is comprised of crystals of calcium phosphate surrounding collagen fibrils. The crystals occur in polycrystalline mineral platelets (MPs). The c-axes of the nanocrystal components of the platelets have an overall preferred orientation parallel to the collagen fibrils but which varies somewhat. In this contribution we show how dark-field (DF) image processing can be used to measure and visualize nanocrystal orientations over micrometer-sized areas. We recorded selected area electron diffraction patterns from ion-beam milled TEM sections of the femora of Wistar rats cut parallel to the collagen fibrils. Diffraction arcs of the 002 reflection represent the variation in the orientation of c-axes of the nanocrystals. Performing DF imaging of electrons from five consecutive, discrete portions along these arcs, we created a series of images. Using a different color coding for each portion, we constructed a merged DF image, which allows intuitive visualization of gradual change of nanocrystal orientation. We show that many complete platelets are built of crystals whose c-axes vary in orientation by up to 26°. In some regions, stacks of platelets have essentially uniform c-axis orientation. These could be "tesselles" which make up only small fraction of volume of bone. Elsewhere adjacent MPs may differ widely (up to 50°) in orientation.

Key words: bone mineral, c-axis orientation, dark-field images, mineral platelets, selected area diffraction, transmission electron microscopy

Introduction

Bone is composed of approximately equal volumes of a mineral (a calcium phosphate) and collagen in the form of fibrils about 50 nanometers (nm) in diameter. Bone mineral (BM) was formerly considered to be nanocrystalline hydroxyapatite of hexagonal $P6_3/m$ symmetry but it has now been shown to be a distinct monoclinic phase of calcium phosphate (Kis et al., 2025).

The ultrastructure of bone has been a continuing topic of inquiry since the late 20th century. With the introduction of the diamond knife for microtomes (Fernandez-Morán & Engström, 1957), it became possible to prepare ~100 nm thick sections for use in transmission electron microscopy (TEM). Many studies were published on this topic (e.g., Arsenault, 1989; Landis et al., 1996; Weiner et al., 1991) and on the apparently related topic of mineralization of avian tendon (Bigi et al., 1988; Siperko & Landis, 2001). In many of these studies at was proposed that BM largely lies in gap zones in collagen fibrils (CF). These are 40 nm-long zones which are repeated every approximately 67 nm along a fibril in which higher electron densities were observed and inferred to be accumulations of mineral, filling gaps between the ends of collinear collagen molecules. We refer to these as mineralized gap zones.

Later studies (Jantou et al., 2009; McNally et al., 2012) found that the use of microtomes in sectioning resulted in severe distortion and disruption of the orientation of mineral structures in bone. This could be avoided through the use of ion-beam milling methods (Boyde, 1974; McNally et al., 2012; Schwarcz, 2015; Schwarcz et al., 2024a, 2024b; Bibko et al., 2025). TEM analyses of sections cut using ion-beam milling showed that bone is made up of plate-shaped nanocrystals which form polycrystalline platelets ~5 nm in thickness (Schwarcz et al., 2014; Kis et al., 2025). These mineral platelets (MPs) surround and lie between CF. Sections of long bones (femora, etc.) oriented so that the CFs are lying in the plane of the section (Fig. 1a) show stacks of MPs passing between the CFs. Sections cut with the CFs oriented normal to the plane of the section (Fig. 1b) allow us to see how the MPs wrap around and lie between the CFs.

We can combine the features shown in Figures 1a and 1b to show, schematically, the arrangement of MPs wrapping around CF (Fig. 2).

Comparison of Figures 1a and 1b show identical electron-dense (black) lines; we inferred that these are edge-wise views of the ~5nm-thick polycrystalline MPs (McNally et al., 2012; Schwarcz et al., 2014). As the MPs are gradually tilted away from an orientation parallel to the electron beam, their electron density decreases with decreasing thickness of the pathway of the electron beam. For this reason as well as possible changes in diffraction-generated contrast, they are practically invisible in bright-field (BF) images such as

Received: December 1, 2025. **Revised:** March 26, 2026. **Accepted:** April 16, 2026

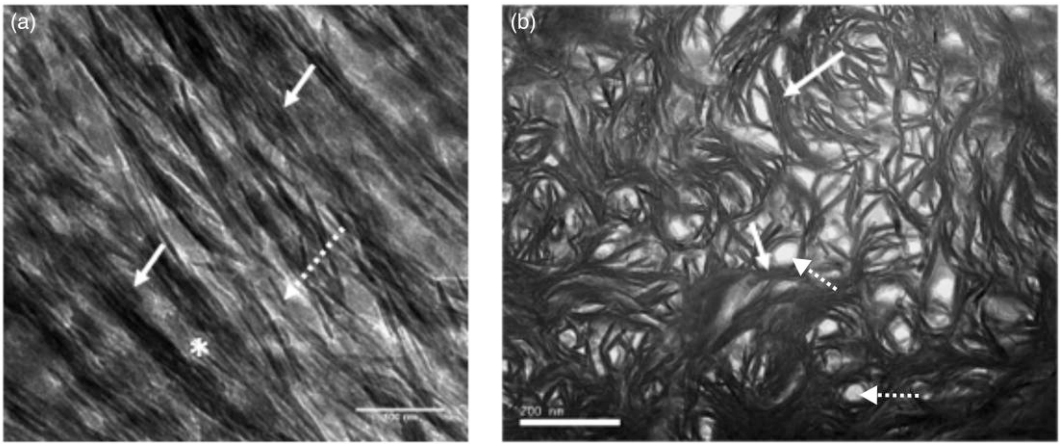

Fig. 1. TEM images of ion-beam milled sections of bone. (**a**) Section of cow femur cut parallel to axes of collagen fibrils; pale dark bands, oriented in strips running from upper left to lower right, are from mineralized gap-zones in fibrils; collagen are otherwise not resolvable in sections cut in this orientation. Oriented parallel to the collagen fibrils are stacks of mineral platelets (MPs) indicated by solid arrows. The dashed arrow indicates one isolated MP. Scale:100 nm; (**b**) section of human femur cut normal to axes of collagen fibrils, showing MPs wrapping around collagen fibrils (dashed arrows) and curved in spaces between fibrils. Arrows: stacks of MPs. Scale: 200 nm.

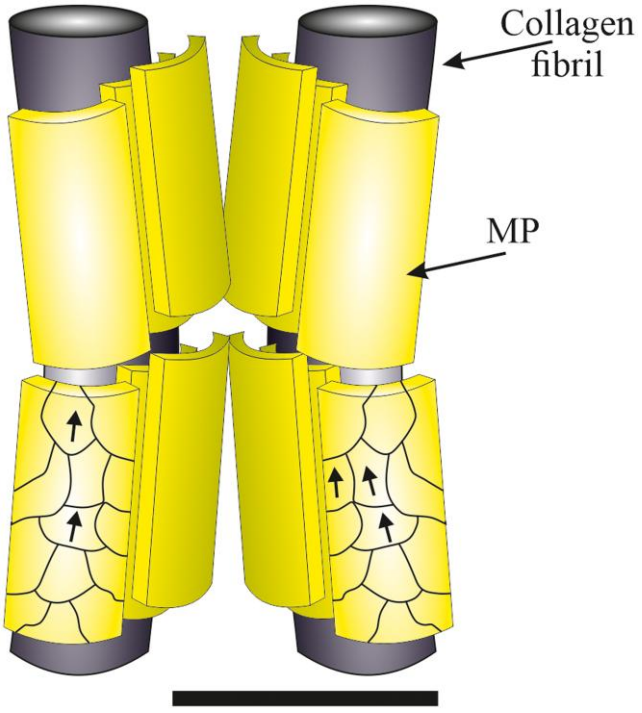

Fig. 2. Schematic drawing showing arrangement of polycrystalline mineral platelets (MP) surrounding and lying between collagen fibrils. Arrows show orientation of **c**-axes in component crystals of MPs. Scale = 100 nm.

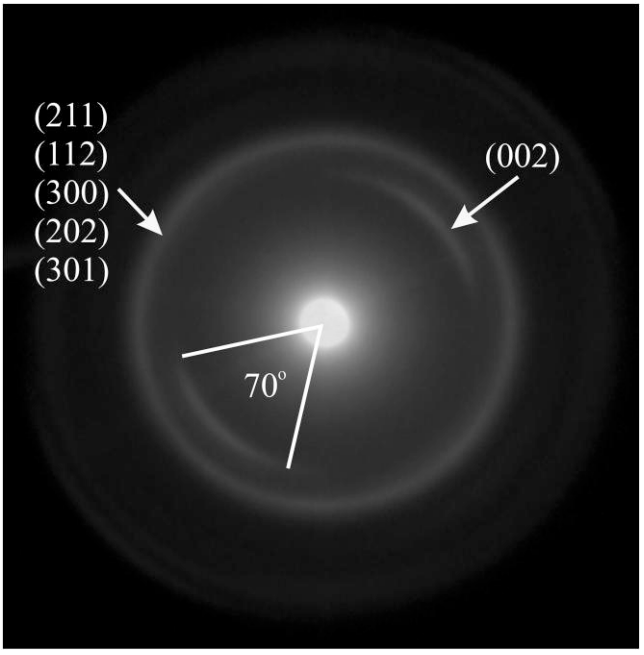

Fig. 3. Selected area electron diffraction (SAED) pattern taken from a TEM section of femur of a Wistar rat cut parallel to the long axes of collagen fibrils. The reflections in the SAED pattern correspond to lattice planes in the BM crystals, identified as shown on figure.

Figures 1a and 1b due to the small contrast when viewed in any other orientation than edgewise (Schwarcz et al., 2024a, 2024b). In Figure 1a flat-lying MPs must also fill the spaces between adjacent stacks of MPs (asterisk) but are unresolvable due to their orientation normal to the electron beam.

In all vertebrates which we have studied (cow, human, pig, etc.) the MPs are gathered in stacks of between 2 and >30 MPs, with spaces <1 nm wide between the closest of them. These stacks are curved into cylindroidal forms which wrap around the CF or extend between them (Schwarcz et al., 2024b), the radius of curvature varying from ~25 nm for those near fibrils, to > 1 μm; some stacks are essentially flat, even when viewed in sections cut perpendicular to CFs. In sections cut parallel to CFs, all MPs appear flat because they are effectively axial sections of cylinders.

Selected area electron diffraction (SAED) patterns recorded from sections of long bones (femora, tibiae, etc.) oriented like Figure 1a (with the CFs in the plane of the section) yield one well-defined diffraction ring as well as two well-defined arcs (Fig. 3).

The pair of arcs lie at positions corresponding to the 002 reflection; they have an angular extent of ~70°. The arcs are always oriented so that their centers lie on a line parallel to the CFs. This has been interpreted as indicating that the **c**-axes of

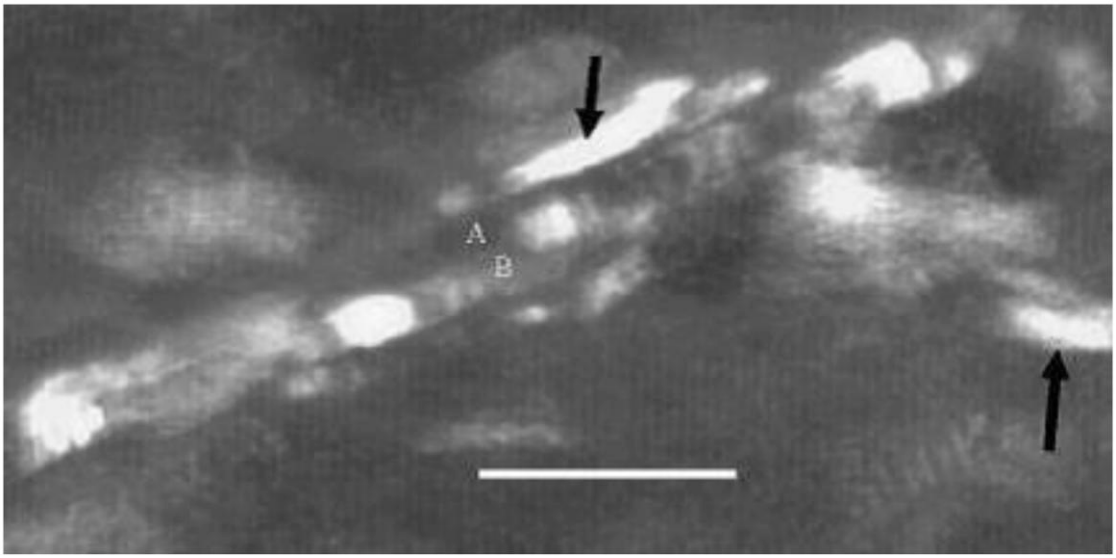

Fig. 4 Dark-field images of a human bone sample of three mineral platelets in a section cut parallel to collagen fibrils, made using electrons from 002 arc. A and B denote two distinct mineral platelets. White (illuminated) volumes (black arrows) are single crystals of BM. Adjacent to them are other crystals in different orientation which do not scatter electrons from the portion of the SAED which was used to generate the dark-field image. Scale = 25 nm. From Schwarcz et al. (2014).

the BM crystals are aligned approximately parallel to the CF axes, possibly because they have crystallized by epitaxial growth on the surfaces of the fibrils (Trautz & Bachra, 1963). Since the SAED pattern includes crystals covering a relatively large sample volume (up to 1.5 μm diameter × 100 nm of sample thickness) within the field of view (FOV) of the TEM images, the spread in the angles of the **c**-axes could be due to differences in orientation of CFs within this volume. This is unlikely because the fibrils are created as discrete bundles with uniform parallel orientation on the scale of 0.5–2 μm (Cassella et al., 1994; Asawa et al., 2004), which is larger than the scale of the SAED. The dispersion could represent variation in the orientation of crystals within individual MPs (see below). We show however, that the crystal orientation within single MPs is quite uniform, varying by $\leq 13^{\circ}$. It seems more likely that the 70° spread represents variation in the orientation of MPs with respect to one another.

It is possible to use the SAED patterns to create images by capturing electrons from a selected portion of the scattering rings and generating a dark-field (DF) image. The only points of illumination in it are at positions in the FOV where a crystal was situated with its **c**-axis oriented consistent with the selected portion of the SAED ring. Figure 4 shows a typical DF image of a sample of human bone (Schwarcz et al., 2014) made using electrons from the 002 arc.

The illuminated (white) areas, discrete patches within the edgewise-viewed MPs, are single crystals of BM. This shows that the MPs are polycrystalline plates. This polycrystalline character is also shown using high-resolution TEM analysis and fast Fourier transform (FFT) analysis of individual MPs which were isolated from bone by chemical oxidation of collagen (Kis et al., 2025). The image in Figure 4 was obtained by setting an aperture on a selected portion of one of the 002 arcs. If we set the spot ("target spot") on a different location on the same arc, we would presumably cause different crystals in the FOV to be illuminated. In this paper we have done this, creating DF images from five points located successively along, and completely covering, single 002 arcs. We reproduce these multiple images in five different colors and then superimpose them on one another to form a single, multicolor DF image representing electrons scattered from the full length of the arc. In this way we can see the angular relationship between the **c**-axes of all the BM crystals which were oriented so that they could be detected in a DF image. We recognize that this will be only a fraction of the total BM crystals in the MPs. Nevertheless, this provides valuable information about the orientation relation of the nanocrystals in the fields of MPs.

Note that we have shown that the individual MPs are assembled from up to 20 or more crystals. In our discussion we shall refer to these components of the MPs as crystals rather than grains or particles. This emphasizes that this is a study of the orientation of individual crystals rather than the plate as a whole.

Materials and Methods

The study involved femurs from two mature female Wistar rats weighing 180–230 g, obtained from a certified supplier. The animals had been used in an ovariectomy experiment as a control group. All procedures with the animals were performed in accordance with the rules and recommendations for the humane treatment of animals used for experimental and other scientific purposes (Order of the Ministry of Health of the Russian Federation dated 01.04.2016 No. 199n "On Approval of the Rules of Good Laboratory Practice"). Animals were euthanized by simultaneous decapitation under CO_2 anesthesia. The femora were then removed for further study.

The long bones of rats do not remodel (Lad, 2023) and therefore do not contain Haversian tubes. Their overall structure is otherwise like that of larger vertebrates.

Two samples from two separate Wistar rats were used in this study, labeled H1 and H2. The bones were cleared of muscle tissue mechanically. The femora were then divided into four sections using a low-speed saw cutting normal to

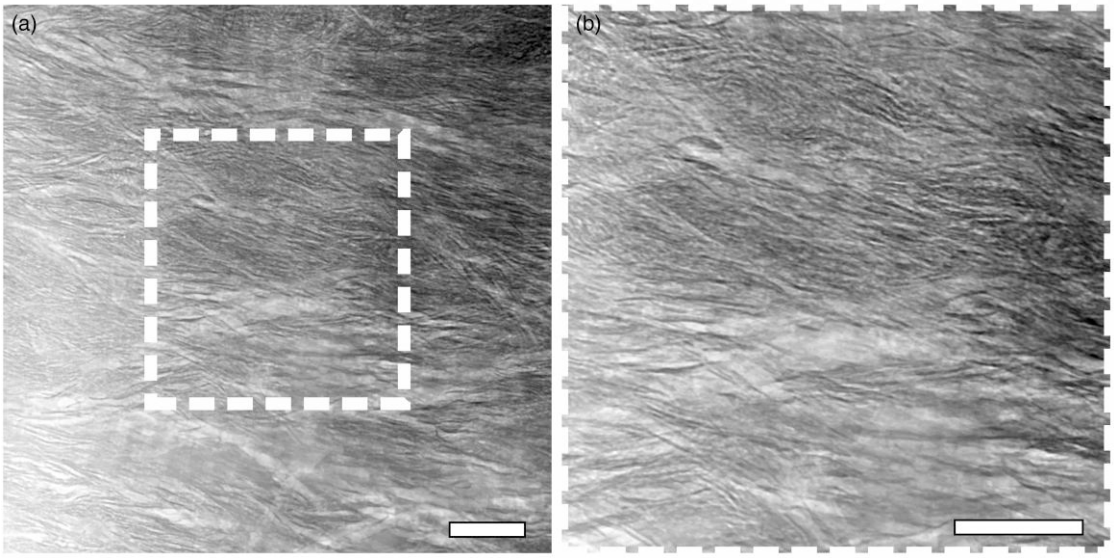

Fig. 5 (**a**) Bright-field TEM of section of bone from Wistar rat cut parallel to the axes of collagen fibrils. (**b**) slightly enlarged view of area defined by dashed lines in a. Bands about 40 nm wide spaced 67nm apart are faintly visible, extending vertically through the entire field of view; these are partially mineralized gap zones in the collagen fibrils. Scale bars in both = 200 nm.

the axis of the femur. First, each section was cut transversely across the bone's elongation, and then each section was cut along the bone's elongation. Next, one random section of each bone was selected and a portion of the diaphysis ~6 mm in length was separated. The diaphysis portion was thinned by grinding on a hard backing. The SiC abrasive was changed when a fixed thickness was reached: down to 1 mm with a grit size of 14 μm, down to 0.4 mm with 7 μm, and down to 0.3 mm with 3 μm. First, the outer side of the diaphysis was ground. Then, the resulting smooth surface was glued to a glass slide for further preparation. Thus, the final specimen was obtained from the middle of the diaphysis wall. It was a rectangular plate about 3 mm × 10 mm. These were mounted in a standard JEOL EM-21010 sample holder for examination in the JEOL 2100.

Further polishing was performed using a Model 200 Dimpling Grinder (Fischione instruments, USA), resulting in the formation of opposing dimples on each side of the sample, with a material thickness of approximately 20 μm between them. The samples were then subjected to ion-beam thinning using a Model 1051 TEM Mill (Fischione instruments, USA) at an accelerating voltage of 3 kV, using an Ar^+ ion beam at an angle of 3° to the surface. This resulted in perforation of the sample at the previously obtained dimples. The samples were pre-coated with carbon and studied along the perforation edges, using a JEM-2100 TEM (JEOL, Japan), equipped with a CCD imaging and diffraction camera, at an accelerating voltage of 200 kV.

A SAED pattern was obtained from an area larger than 1.5 μm^2. This showed the diffraction pattern of apatite in which the 002 reflection was in the form of an arc with an angular extent of about 70°. The objective aperture was sequentially placed at five discrete points on the 002 arc selected so that no empty spaces remained on the arc. A DF image of an area 1.5 × 1.5 μm was obtained using each point, with an exposure of 100 s. Care was taken not to disturb the setting of the sample between exposures.

The resulting DF images were converted from black and white to red, blue, cyan, green, and yellow for each point on the 002 arc. The resulting images were superimposed using an image-merging mode ("Addition"), producing a single, multicolor DF image.

Results and Discussion

Section H1

Three fields of view were studied from near the middle of the slice of cortical bone. All sections were oriented parallel to the CF axes. We shall first discuss the bright-field images of each FOV and then discuss the colored DF images obtained of the same areas.

Bright Field Images

Figure 5 shows a typical BF image of one of the areas, Area 3.

As in Figure 1a, the FOV is filled with edgewise images of MPs aligned parallel to the CF. The presence of the collagen is shown by the faint 40 nm dark bands of the partially mineralized gap zones. Unlike Figure 1a, there are no obvious gaps between stacks of MPs. This may be due to differences in the 3D arrangement of MPs which has not yet been investigated in rats or other small rodents where this pattern is observed.

Dark Field Views

Three fields of view were obtained using five target spots on one of the 002 arcs, as shown in Figure 6.

Dark-field images were produced using each target spot, and then merged to produce a complete DF FOV. Three images were obtained labeled CR 1, CR 2 and CR 3, corresponding to three fields of view. In Figure 7, each colored field is shown together with the corresponding BF view of the same FOV. The orientation of crystals with a particular color is determined with a precision of ± ~7° (corresponding to the angular width of the spot).

General Overview

In each DF image we can see that MPs are outlined by arrays of uniformly colored, elongate rectangular spots. These are

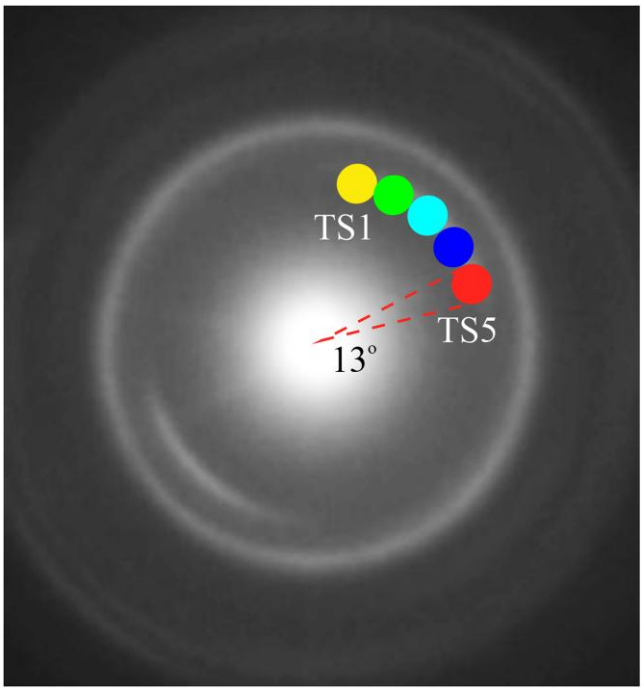

Fig. 6. Target spots on 002 arc colored as used to identify MPs in DF images. Target spots are numbered TS1 to TS5. Each spot covers an angular range of ~13°.

arrays of crystals within single MPs. The uniformity in color of the crystals along the length of single MPs tells us that the lattice orientation of crystals is approximately uniform for the length of the MP, and the orientation difference does not exceed 13°. This is in agreement with FFT analysis of high-resolution TEM images of single MP (Kis et al., 2025). Because the crystals within single MPs are discrete, there must be some difference in their orientation. This has been studied by Kis et al. (2025) who suggest that the crystals are slightly rotated around their **c**-axes, while the **c**-axes are all approximately co-aligned. We discuss this later.

While we cannot precisely identify particular MPs in the BF image that have been illuminated in the DF image, the orientation of the MPs in any given region of the FOV agrees in the BF and DF images. In the BF image we see structures consisting of MPs attached end to end, which form extended arrays. In sections cut normal to CFs we see these arrays are parts of columns whose wall are built of MPs and which extend hundreds of nm or more parallel to the CFs (Idkaidek et al., 2021). These contribute to the stiffness of bone with respect to twisting or bending. Due to the existence of these extended arrays, it is difficult to identify a specific MP discernible in a DF image of the same FOV.

The fields of view contain crystals with orientations spanning the entire range of the arc of the 002 reflection. Fields CR1 and CR3 mainly contain crystals from the inner three sectors TS 2, 3, and 4 while CR2 also contains many TS5 crystals.

Lengths of Platelets and Crystals

Coloring of the MPs allows us to make more careful measurements of the dimensions of the MPs and of their component crystals (Table 1). The plate lengths are for the portions of the plates and crystals that had been captured within the ~100 nm thick TEM section; the remainder of some MPs and crystals could be larger than is represented here. Figure 8 shows a detail of image CR 2 in which we can see more clearly the lengths and rectangular shapes of the crystals which comprise the MPs.

The average length of the MPs ranges from 142 to 198 nm. The maximum dimension of MPs in each CR image is up to twice the average for that CR; the average of the maxima for all three CRs is 319 ± 87 nm which would be an estimate of the maximum size of the MPs in this bone.

Crystals within each MP average between 23 and 30 nm in length; their maximum value averages 43 ± 9 nm. The crystals tend to be oriented parallel to their c-axes so this should be similar to their true lengths parallel to the **c**-axis. Using the Scherrer method on the 002 peak in X-ray diffraction, the mean of crystal lengths in rat bone was found to be about 34 nm (Turunen et al., 2016) although the measurements did not extend as high as 40 nm.

Variation in Crystal Orientation Within and Between MPs

In Figures 1a and 1b, MPs are oriented closely parallel to one another in a single plane, forming stacks of platelets which are also visible in the colored images. The colored images show that the 70° angular spread of the 002 arc in the SAED pattern reflects both variation in orientation of the c-axes within those planes and also difference in orientation of **c**-axes in different MP. From the variation in color between adjacent MPs, we see that they can have markedly different angles for their component crystals (Fig. 7). As each color defines crystal orientation with a precision of $\pm 7°$, we cannot define the variation in orientation within single MPs more precisely than that. However it is clear that crystals within MPs vary in orientation to greater extent than 7° Some large areas have little variation in color but even within these the orientation of the individual crystals can vary significantly. CR3, for example, contains a large area which is uniformly the colors of TS3 and TS4. This is because adjacent crystals within single MPs are illuminated by either TS3 or TS4 (Fig. 9).

Each TS has an angular width of about 13° (Fig. 6). Therefore, the maximum possible angular width covered by the crystals within one MP that spans two TS's such as those in CR3 would be ~26°.

In each CR we found some MPs which contain nanocrystals that scatter electrons into two adjacent TS's (Fig. 10).

The angular spread between adjacent crystals in a single MP is always between two adjacent TS's.

Adjacent MPs can have crystals with larger orientation differences (Fig. 11).

An area in Figure 9, about 1 μm in length, contains many MPs whose crystals are oriented approximately parallel to one another (although illuminated by two TSs). This represents a stack of MPs, all with similar **c**-axis orientation. It is the only example of such a stack in the images in the present set of CRs. However, BF images (Fig. 7) show many stacks of MPs within the FOV. It appears that it is less common for the MPs in these stacks to have uniformly oriented **c**-axes. That is seen more commonly in the H2 section, discussed next.

Sample H2

Figure 12 shows BF and DF images of a section of a femur from another Wistar rat. The same target spots were used to color the sub-regions of the 002 arc.

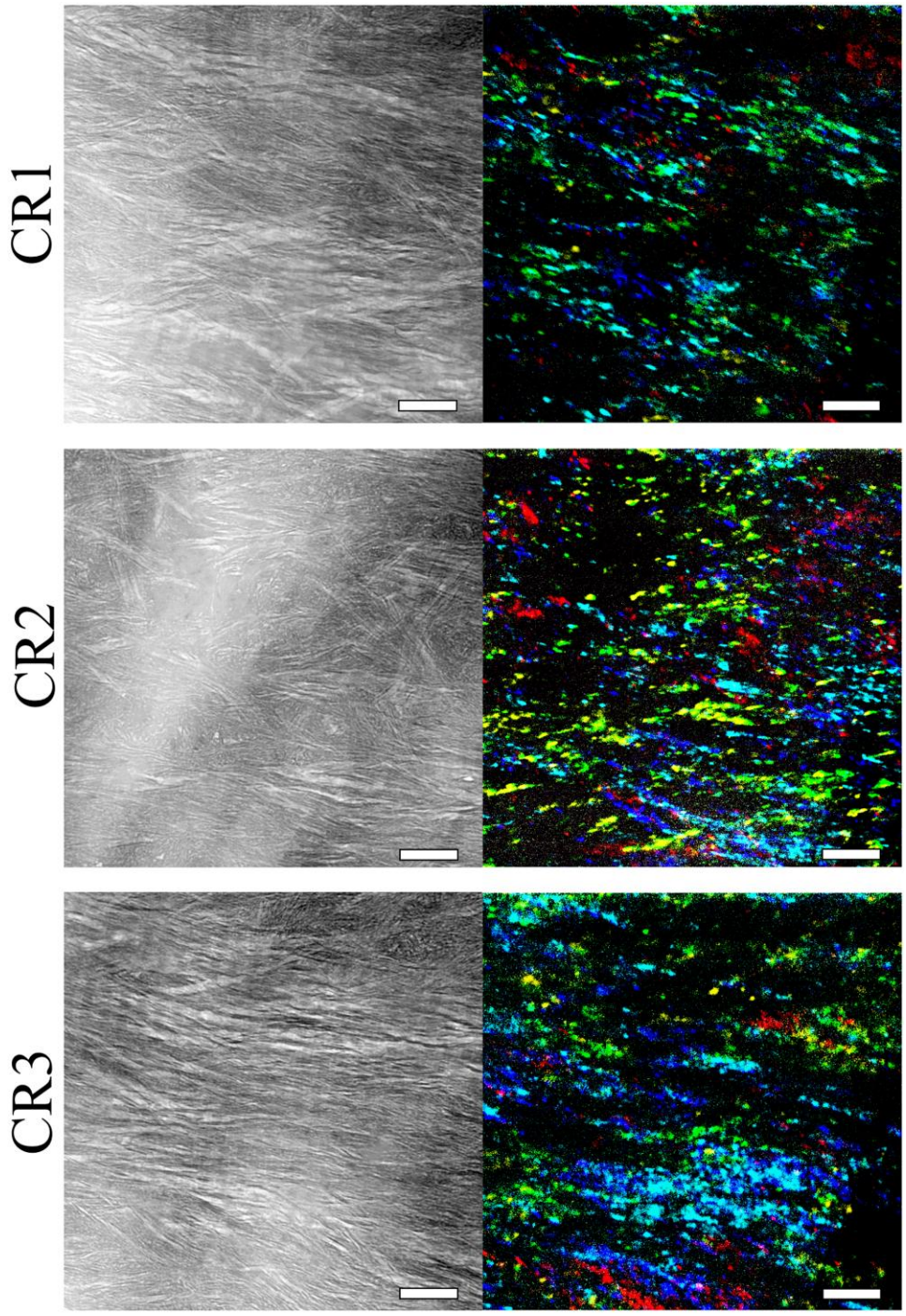

Fig. 7. Bright-field (BF) and dark-field (DF) images of same field of view, with DF images colored according to target spot colors in Figure 6. Scale = 200 nm.

Table 1. Lengths of Mineral Platelets (MPs) and of Crystals Within Them, in Nanometers (nm).

	MPs			Crystals		
CR	Ave	Sd	max	Ave	Sd	max
1	142	57	231	23	5	33
2	181	110	405	30	10	48
3	192	81	320	27	9	49
Ave			319	27		43
Sd			87			9

Max, maximum length of crystal or platelet.

In Figure 12b we see two regions approximately 400 nm long and a few hundred nm wide in which all the crystals have the same crystal orientation. Within single MPs, electrons from two adjacent TSs are present implying an internal spread of 26°.

Completeness of MPs

Colored DF images of some MPs are completely filled with patches representing adjacent TSs on the 002 arc. As a result, we can see almost the complete form of the MP. Those MPs

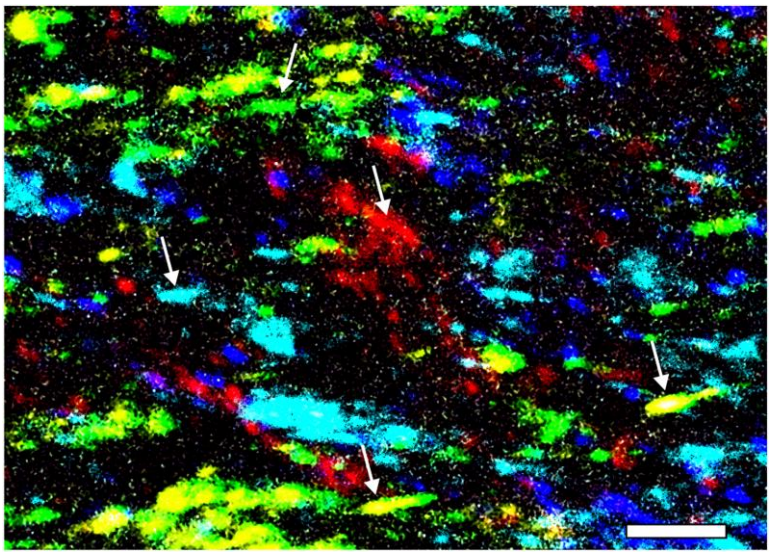

Fig. 8. Detail of image CR2 showing shapes and sizes of a few individual crystals marked with arrows.

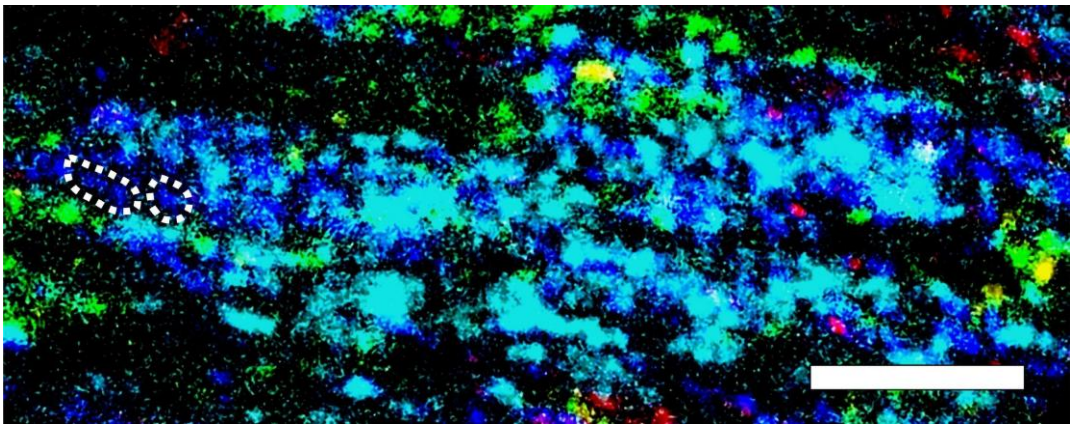

Fig. 9. Area of CR3 in which all the crystals are colored by TS3 or TS4. Dashed lines outline two adjacent crystals in TS4 orientation. Scale = 200 nm.

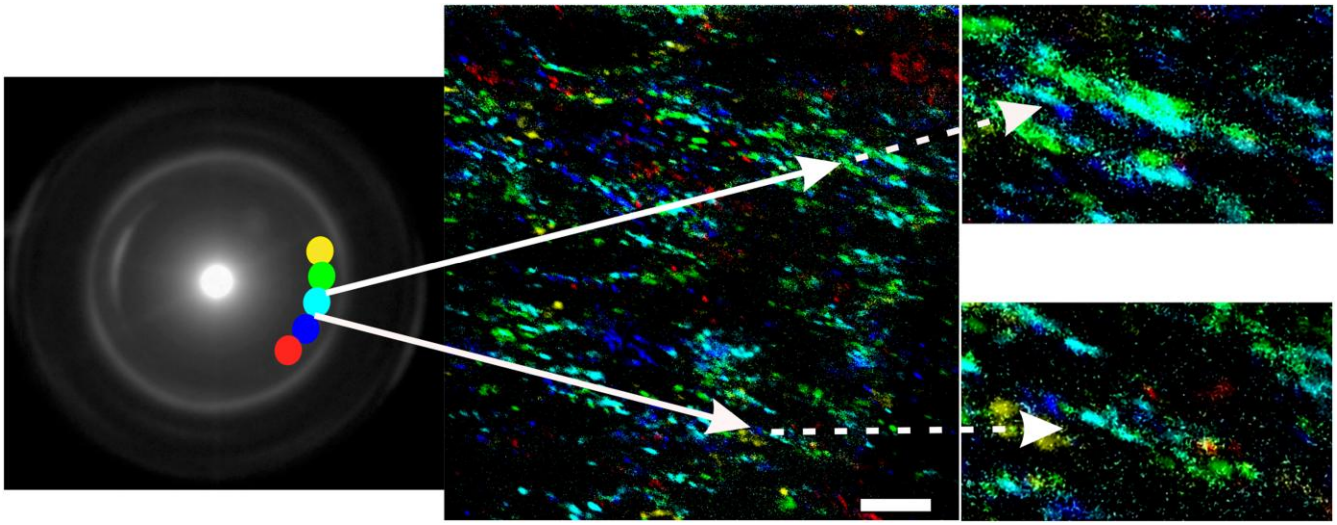

Fig. 10. Details of CR1: adjacent crystals in same MP with significant angle differences. The white arrows connect the crystals to the junction between two TS's which are illuminating crystals of the MP; scale = 200 nm. Figures on right, connected with dashed arrows, show details of the multiple orientations within the single MPs; scale = 100 nm.

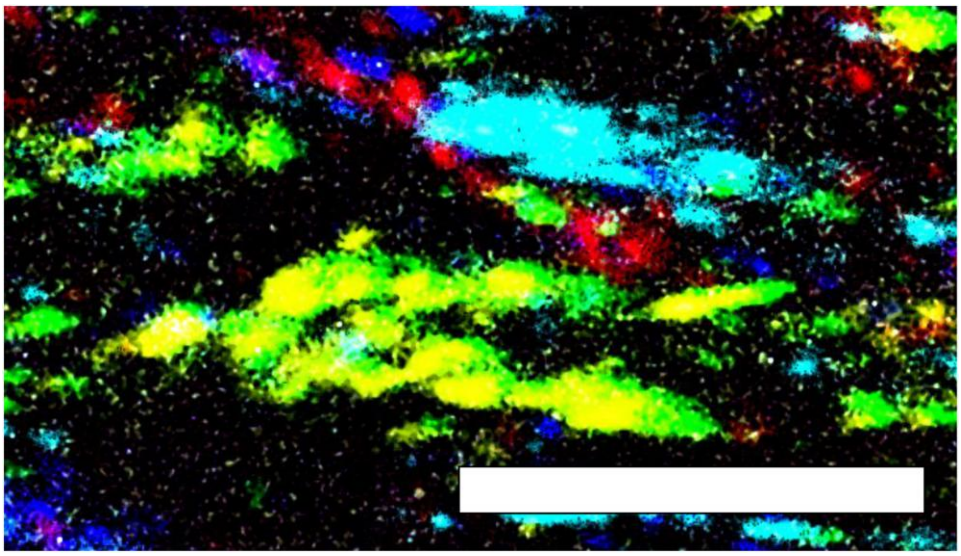

Fig. 11. Detail of CR2 showing MPs illuminated by TS 1 and TS2 and adjacent MPs with different orientations; scale = 200 nm.

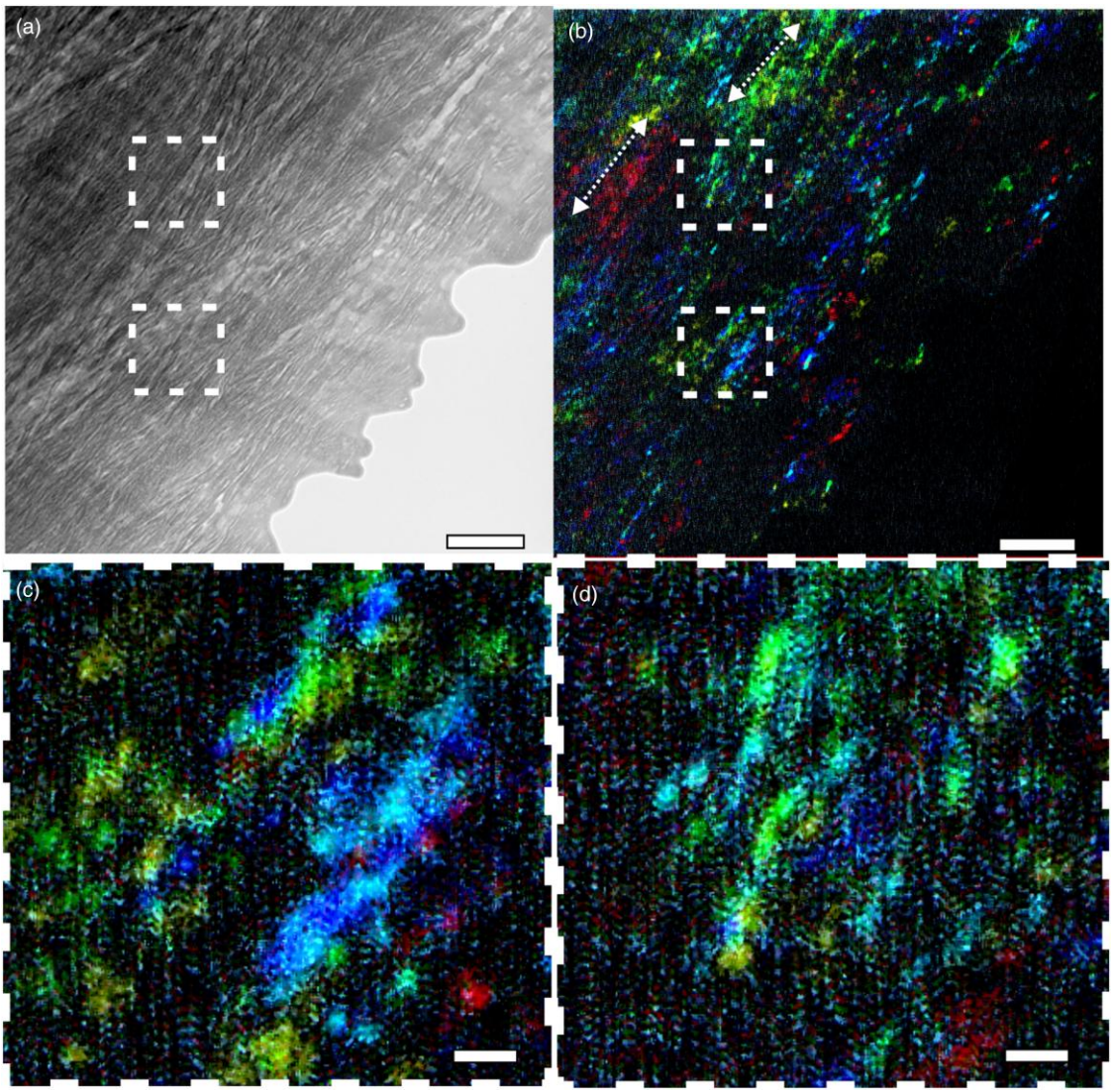

Fig. 12. Bright-field (**a**) and dark-field (**b**) images of a field of view of a femur of another Wistar rat H2; double-headed arrows: large regions of uniformly oriented crystals; white squares mark regions in each image; (**c**, **d**) details of lower square (**c**) and upper (**d**) showing variation in TS between adjacent crystals within MPs: scales: 200 nm for (**a, b**) and 50 nm for (**c**, **d**).

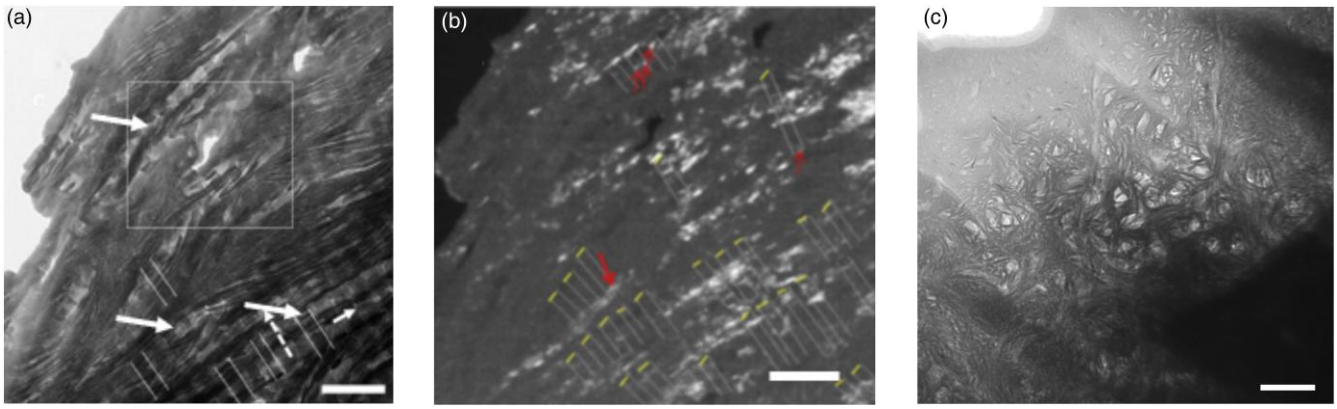

Fig. 13. A bright-field TEM image of FIB section of human femur cut parallel to collagen fibrils, showing stacks of mineral platelets surrounding collagen fibrils (arrows); (**b**) dark-field image of same area using only one portion of the 002 arc. Note dark areas which coincide with positions collagen fibrils; MPs are also present there but lying flat in the plane of the section. Scale = 200 nm; images and (**b**) from Schwarcz et al. (2020); (**c**) bright-field image of ion-milled section of rat bone studied in this paper cut normal to axes of CFs; areas of collagen fibrils appear as light-colored circles; sections of these CFs are only faintly visible in sections cut parallel to CFs (Fig. 7); scale = 100 nm.

that contain dark patches contain crystals in which the c-axis is not in the image plane so that electrons diffracted from the 002 lattice planes are not detected on the SAED (Fig. 7).

Dark Areas

Crystals of BM are made visible (illuminated) in sections of MPs when they are oriented so that the plane of the crystal plate is normal to the plane of the section. Large dark areas in the DF images represent areas where no such edgewise views of MPs are present at all. Schwarcz et al. (2020) show a clearer example of this from a section of human bone where the stacks of MPs are more visibly interrupted by elongate zones where gap zones in CFs are clearly visible (Fig. 13a). Here the section cuts through a CF surrounded by stacks of MPs.

In the rat bones studied here, the CF are less apparent, possibly, because they have less Ca and PO_4 in the gap zones than those in Figure 13a. However, areas totally lacking in illuminated images of BM crystals elongated parallel to the MPs should represent areas where CF dominate and the 5 nm thick MPs were lying almost flat in the section.

Conclusions

We have shown DF maps produced by electrons from multiple target points on the 002 arc of a SAED, for three areas in one bone sample and one region in another sample. The crystals visualized by the five discrete parts of the 002 arc are illuminated in five discrete colors and then synthesized into a single image. In these images we see that, for some MPs, the entire platelet is illuminated, but with different colors appearing along the length of the MP. No single MP is completely illuminated in a single color. Pairs of colors are always generated by adjacent target spots on the 002 arcs, implying gradual variation in the angle of the **c**-axis of nanocrystals by up to 26° inside a mineral platelet. In one region of one image, many adjacent MPs display the same adjacent pairs of colors, showing that this is a stack of homogeneously oriented MPs. In other locations adjacent MPs differ in **c**-axis orientation by up to 50°, showing an overall inhomogeneous pattern of **c**-axis orientation.

The patches of homogeneously oriented MPs are on the order of 1 μm in length and less than this in width (normal to the MPs). They somewhat resemble the ellipsoidal clusters of mineral observed at mesoscale using FIB-SEM (Binkley et al., 2020); these features are described as "cross-fibril mineral tessellation" by Buss et al. (2020) although it is not clear how any cluster of crystals could cross through a fibril. The detailed connection between "mineral tessellation" and homogeneously oriented stacks of MPs could be a subject of future investigations combining SEM and DF TEM studies of the same samples. However, patches of close-spaced angularly homogeneous MPs were not common.

The approximate homogeneity of orientation of crystals within MPs is not surprising in itself as it is implicit in the high-resolution TEM studies of isolated MPs (Kis et al., 2025). We showed here that within single 2.25 μm^2 areas of ion-beam milled sections of cortical bone there is varying orientation in some areas, and homogeneous orientation in others. These features are presumably relevant to the "design" of bone to optimize its strength and toughness.

We are only able to examine these characteristics in sections cut parallel to the axes of CF. However, much of the "design" of bone is more apparent in sections cut at 90° to these, where we can see MPs wrapping around and curving between CF. But in this orientation, we are not able to see individual crystals inside MPs, which was the goal of this study.

Throughout this paper, we have referred to the mineral of bone as "BM". Its structural features were described by Kis et al. (2025). This phase is apparently not a mineral since it has not yet been identified as a geological mineral. No name has been given to it yet so we are obliged to refer to it as BM.

Availability of Data and Materials

The authors have declared that no datasets apply for this piece.

Author Contributions Statement

Conceptualization and investigation: A.B.; Visualization: A.B. and H.S.; Writing—original draft: H.S.; Writing—review and editing: A.B., H.S., and V.K.

Acknowledgments

The TEM investigations have been carried out using the equipment of Share Use Centre "Nanotech" of the ISPMS SB RAS.

Financial Support

No research funds were received to support this study.

Conflict of Interest

The authors have no conflicts of interests regarding any material presented in this paper.

References

Arsenault AL (1989). A comparative electron microscopic study of apatite crystals in collagen fibrils of rat bone, dentin and calcified Turkey leg tendons. *Bone Miner* **6**(2), 165–177. https://doi.org/10.1016/0169-6009(89)90048-2

Asawa Y, Aoki K, Ohya K, Ohshima H & Takano Y (2004). Appearance of electron-dense segments: Indication of possible conformational changes of pre-mineralizing collagen fibrils in the osteoid of rat bones. *J Electron Microsc (Tokyo)* **53**, 423–433. https://doi.org/10.1093/jmicro/dfh057

Bibko AA, Bukharova OV, Shendrik RY, Schwarcz HP, Lychagin DV & Kostrub EA (2025). Chemical composition and ultrastructure of bone apatite in initial osteoporosis: Mineralogical study. *Crystals* **15**, 1057. https://doi.org/10.3390/cryst15121057

Bigi A, Ripamonti A, Koch MHJ & Roveri N (1988). Calcified Turkey leg tendon as structural model for bone mineralization. *Int J Biol Macromol* **10**, 282–286. https://doi.org/10.1016/0141-8130(88)90005-0

Binkley DM, Deering J, Yuan H, Gourrier A & Grandfield K (2020). Ellipsoidal mesoscale mineralization pattern in human cortical bone revealed in 3D by plasma focused ion beam serial sectioning. *J Struct Biol* **212**, 107615. https://doi.org/10.1016/j.jsb.2020.107615

Boyde A (1974). Transmission electron microscopy of ion beam thinned dentine. *Cell Tissue Res* **152**, 543–550. https://doi.org/10.1007/BF00218937

Buss DJ, Reznikov N & McKee MD (2020). Crossfibrillar mineral tessellation in normal and Hyp mouse bone as revealed by 3D FIB-SEM microscopy. *J Struct Biol* **212**, 107603. https://doi.org/10.1016/j.jsb.2020.107603

Cassella JP, Barber P, Catterall AC & Ali SY (1994). A morphometric analysis of osteoid collagen fibril diameter in osteogenesis imperfecta. *Bone* **15**(3), 329–334. https://doi.org/10.1016/8756-3282(94)90296-8

Fernandez-Morán H & Engström A (1957). Electron microscopy and x-ray diffraction of bone. *Biochim Biophys Acta* **23**, 260–264. https://doi.org/10.1016/0006-3002(57)90327-X

Idkaidek A, Schwarcz H & Jasiuk I (2021). Modeling of bending and torsional stiffnesses of bone at sub-microscale: Effect of curved mineral lamellae. *J Biomech* **123**, 110531. https://doi.org/10.1016/j.jbiomech.2021.110531

Jantou V, Turmaine M, West GD, Horton MA & McComb DW (2009). Focused ion beam milling and ultramicrotomy of mineralised ivory dentine for analytical transmission electron microscopy. *Micron* **40**, 495–501. https://doi.org/10.1016/j.micron.2008.12.002

Kis VK, Schwarcz HP, Nassif N & Szekanecz Z (2025). Bone mineral platelets are mesocrystals formed by monoclinic nanocrystals. *Commun Mater* **6**, 1–8. https://doi.org/10.1038/s43246-025-00890-4

Lad SE (2023). Absence of secondary osteons in femora of aged rats: Implications of lifespan on Haversian remodeling in mammals. *J Morphol* **284**, e21600. https://doi.org/10.1002/jmor.21600

Landis WJ, Hodgens KJ, Arena J, Song MJ & McEwen BF (1996). Structural relations between collagen and mineral in bone as determined by high voltage electron microscopic tomography. *Microsc Res Tech* **33**, 192–202. https://doi.org/10.1002/(SICI)1097-0029(19960201)33:2<192::AID-JEMT9>3.0.CO;2-V

McNally E, Schwarcz H, Botton G & Arsenault A (2012). A model for the ultrastructure of bone based on electron microscopy of ion-milled sections. *PLoS One* **7**, e0029258. https://doi.org/10.1371/journal.pone.0029258

Schwarcz H, Micheletti C & Grandfield K (2024a). Effect of plate orientation on apparent thickness of mineral plates by transmission electron microscopy. *J Bone Miner Metab* **42**, 344–351. https://doi.org/10.1007/s00774-024-01507-5

Schwarcz HP (2015). The ultrastructure of bone as revealed in electron microscopy of ion-milled sections. *Semin Cell Dev Biol* **46**, 44–50. https://doi.org/10.1016/j.semcdb.2015.06.008

Schwarcz HP, Binkley DM, Luo L & Grandfield K (2020). A search for apatite crystals in the gap zone of collagen fibrils in bone using dark-field illumination. *Bone* **135**, 115304. https://doi.org/10.1016/j.bone.2020.115304

Schwarcz HP, McNally EA & Botton GA (2014). Dark-field transmission electron microscopy of cortical bone reveals details of extrafibrillar crystals. *J Struct Biol* **188**, 240–248. https://doi.org/10.1016/j.jsb.2014.10.005

Schwarcz HP, Nassif N & Kis VK (2024b). Mineral curved platelets in bone. *Acta Biomater* **183**, 201–209. https://doi.org/10.1016/j.actbio.2024.05.047

Siperko LM & Landis WJ (2001). Aspects of mineral structure in normally calcifying avian tendon. *J Struct Biol* **135**, 313–320. https://doi.org/10.1006/jsbi.2001.4414

Trautz R & Bachra BN (1963). Oriented precipitation of inorganic crystals. *Arch Oral Biol* **8**, 601–613. https://doi.org/10.1016/0003-9969(63)90075-X

Turunen MJ, Kaspersen JD, Olsson U, Guizar-Sicairos M, Bech M, Schaff F, Tägil M, Jurvelin JS & Isaksson H (2016). Bone mineral crystal size and organization vary across mature rat bone cortex. *J Struct Biol* **195**, 337–344. https://doi.org/10.1016/j.jsb.2016.07.005

Weiner S, Arad T & Traub W (1991). Crystal organization in rat bone lamellae. *FEBS Lett* **285**, 49–54. https://doi.org/10.1016/0014-5793(91)80722-F